

## Spin-flip and acoustic-phonon Raman scattering in CdS nanocrystals

A. A. Sirenko,\* V. I. Belitsky, T. Ruf, and M. Cardona

*Max-Planck-Institut für Festkörperforschung, Heisenbergstrasse. 1, 70569 Stuttgart, Germany*

A. I. Ekimov

*A. F. Ioffe Physical Technical Institute, 194021 St. Petersburg, Russia*

C. Trallero-Giner

*Department of Theoretical Physics, Havana University, 10400 Havana, Cuba*

(Received 22 December 1997)

We report on spin-flip Raman scattering and on Raman scattering by acoustic phonons in CdS nanocrystals embedded in a glass matrix. We discuss both the spin-flip and the acoustic-phonon Raman spectra on the basis of the interaction of size-quantized electronic excitations with nonconfined acoustic vibrations. The polarization of spin-flip Raman scattering in the Faraday and Voigt configurations is analyzed in comparison with that for bulk CdS. The effective electron  $g$  factor has been measured as a function of the quantum dot size. [S0163-1829(98)03828-4]

### I. INTRODUCTION

Spin-flip Raman scattering (SFRS) was first studied in bulk CdS by Thomas and Hopfield.<sup>1</sup> The effective  $g$  factors for bound donors and acceptors were measured, and an impurity-mediated spin-flip mechanism was discussed. A variety of other experimental findings, many of which were a direct result of high-resolution SFRS spectroscopy in CdS, was reviewed by Geschwind and Romestain<sup>2</sup> and Scott.<sup>3</sup> Recently, low-dimensional systems such as GaAs/Al<sub>x</sub>Ga<sub>1-x</sub>As (Refs. 4–7) and CdTe/Cd<sub>x</sub>Mg<sub>1-x</sub>Te (Ref. 8) multiple quantum wells and InP/In<sub>x</sub>Ga<sub>1-x</sub>P self-assembled quantum dots<sup>9</sup> have been studied by SFRS in order to obtain information about  $g$  factors. In comparison to other techniques, such as polarized exciton luminescence,<sup>10</sup> optically detected spin resonance,<sup>11</sup> or Hanle effect measurements,<sup>12,13</sup> which only yield the  $g$  factors of either excitons, electrons, or holes, SFRS allows one to determine all these quantities in a single experiment.<sup>4,7</sup>

In the present work SFRS is applied to CdS quantum dots (QD's) embedded in a glass matrix. This system is currently of great interest because of its unique electronic and optical properties, which are modified by size quantization of the electronic states.<sup>14–17</sup> Here we investigate changes of the electron  $g$  factor with the quantum dot size, as well as the polarization and the mechanisms of the SFRS. In this context, the interaction between electronic excitations and acoustic phonons in the case of complete carrier confinement and the nature of the acoustic-phonon spectrum, which can be obtained by Raman spectroscopy, are important to understand our experimental results.

While the optical vibrational modes in QD's based on II-VI semiconductors were extensively studied by means of Raman spectroscopy and their confinement was established both experimentally and theoretically,<sup>17–23</sup> the situation for acoustic phonons is less clear. Distinct maxima (one or two) in the low-frequency Raman spectra around 5–20 cm<sup>-1</sup> were observed in a number of experiments<sup>17,24–26</sup> for differ-

ent nanocrystals embedded in a matrix. It was found that a decrease of the QD radius,  $a^*$ , results in an increase of their Raman shift,  $\Delta^{\max}$ . To explain these maxima, the idea of acoustic-phonon confinement was invoked.<sup>24–28</sup> Eigenfrequencies of spheroidal and torsional confined acoustic modes were calculated using the macroscopic theory of elastic vibrations for a homogeneous spherical body<sup>29</sup> with a free surface, which was assumed to be applicable to nanocrystals.<sup>24–28,30</sup> This macroscopic model describes the dependence of  $\Delta^{\max}$  on  $a^*$  and the polarization of the Raman spectra by means of the interaction with the lowest confined acoustic modes for ‘‘free-standing’’ and ‘‘rigid’’ boundary conditions<sup>28</sup> as well as for the case when the influence of the matrix is taken into account by means of a ‘‘relaxed surface layer.’’<sup>30</sup> The samples used for studies of the acoustic-phonon Raman spectra usually contain nanocrystals embedded in a matrix.<sup>17,24–26</sup> Many different situations, depending on the glass and QD parameters, can therefore occur, in principle, and the modes involved can vary from almost confined to bulklike. However, since the sound velocities in a glass matrix and crystalline CdS are similar, bulklike nonconfined acoustic vibrations are expected to play an essential role in the explanation of the low-frequency Raman spectra for the system that is investigated here. We therefore examine the spectra of acoustic-phonon Raman scattering (APRS) in CdS QD's and propose that the low-frequency maxima in the regime of size-selective excitation appear due to the interaction of size-quantized electronic excitations with nonconfined bulklike acoustic phonons.

### II. EXPERIMENT

Samples with CdS nanocrystals embedded in a glass matrix were grown using a diffusion-controlled phase decomposition of solid solutions. This process has been described in detail by Ekimov.<sup>17</sup> In transmission electron microscopy, the CdS particles show a spherical shape and a nearly perfect wurtzite crystal structure. It is assumed that the nanocrystals

have a random distribution of the  $c$  axis direction in the glass matrix. The mean radius  $\bar{a}$ , of the nanocrystals (not equivalent to  $a^*$ , which is probed under size-selective excitation<sup>17</sup>) has been estimated by comparison of the low-energy absorption threshold position, which is modified due to the carrier confinement, with calculations.<sup>17</sup> For Raman measurements, we used samples with mean dot radii of 33, 44, 70, and 87 Å, comparable to or larger than the bulk exciton Bohr radius of about 30 Å.<sup>31</sup> The regimes of either intermediate or weak exciton confinement are realized in these samples. It was estimated that for each sample the ratio of the mean deviation in the size distribution to the mean radius is about  $0.4 \pm 0.1$ .<sup>17</sup> The samples are polished platelets ( $5 \times 5$  mm<sup>2</sup>) with a thickness of about 0.5 mm. In the following, the samples are labeled by their mean dot radii.

A number of Ar<sup>+</sup>-ion laser lines was used to excite Raman spectra within the energy distribution of excitons confined in the QD's with a certain average size. Following the concept of *size-selective excitation*,<sup>17,21</sup> we assume that only the nanocrystals with an exciton transition energy close to that of the laser are resonantly excited. The excitation power density of the laser was less than approximately 10 mW/cm<sup>2</sup> in order to reduce the local heating of the samples. The sample temperature was varied between 10 and 280 K. It was controlled with a Si diode attached to the sample holder.

Raman spectra were measured with a SPEX 1404 double monochromator equipped with a cooled GaAs photomultiplier for single-photon counting. The resolution limit of our setup is about 0.2 cm<sup>-1</sup>. The experiments were performed in backscattering geometry. Magnetic fields  $B$  up to 14 T were applied both along (Faraday configuration,  $\mathbf{B} \parallel \mathbf{k}$ ) and perpendicular (Voigt configuration,  $\mathbf{B} \perp \mathbf{k}$ ) to the direction of the laser beam  $\mathbf{k}$ .

To investigate polarization effects in the Raman spectra we used the parallel,  $z(x,x)\bar{z}$ , and crossed,  $z(x,y)\bar{z}$ , geometries for linearly polarized measurements, as well as circularly polarized,  $z(\sigma^\pm, \sigma^\pm)\bar{z}$ , and depolarized,  $z(\sigma^\pm, \sigma^\mp)\bar{z}$ , configurations. The first (second) symbol in brackets corresponds to the polarization of the exciting (backscattered) light. The symbols  $x$ ,  $y$ , and  $z$  are not related to the crystallographic axes of the QD's, but represent orthogonal axes with respect to the laboratory frame. For  $\mathbf{k} \parallel z$ ,  $\sigma^\pm = (\mathbf{e}_x \pm i\mathbf{e}_y)/\sqrt{2}$ , where  $\mathbf{e}_x$  and  $\mathbf{e}_y$  are unit vectors along the  $x$  and  $y$  axes. The degree of linear (circular) polarization of the scattered radiation propagating along the  $z$  direction is defined as

$$\rho_{l(c)} = \frac{I_{\parallel} - I_{\perp}}{I_{\parallel} + I_{\perp}},$$

where  $I_{\parallel}$  and  $I_{\perp}$  are the intensities of the light polarized parallel and perpendicular with respect to the polarization of the excitation. For circular polarization  $I_{\parallel}$  ( $I_{\perp}$ ) is the light intensity in the polarized (depolarized) configuration.

The photoluminescence (PL) and absorption spectra of CdS QD's have been systematically studied.<sup>17</sup> Figure 1 shows transmission spectra of the 33, 44, 70, and 87 Å QD's at  $T=10$  K. With decreasing QD size the high-energy threshold in the transmission shifts towards higher energies, corresponding to increasing exciton confinement.

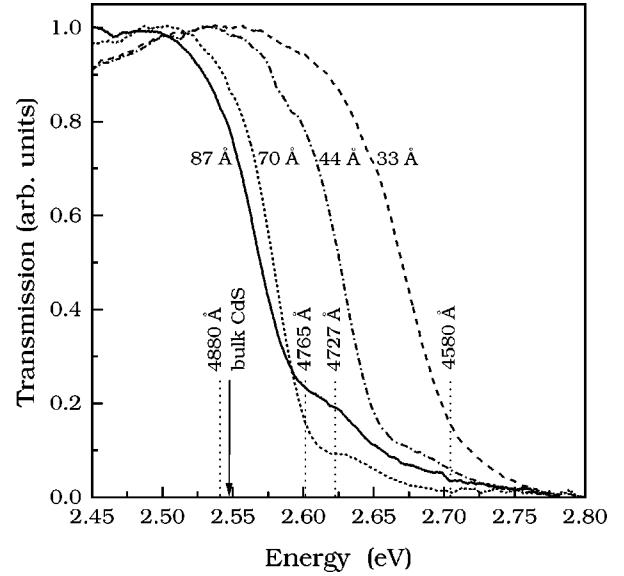


FIG. 1. Normalized transmission spectra of 33, 44, 70, and 87 Å CdS QD's at  $T=10$  K. The laser energies used for size-selective excitation of APRS and SFRS spectra are indicated with dotted lines. The arrow marks the photoluminescence maximum of bulk CdS.

### III. EXPERIMENTAL RESULTS

#### A. Acoustic-phonon Raman spectra at $B=0$

Typical low-frequency APRS spectra for the 33, 70, and 87 Å samples excited with different laser lines are shown in Fig. 2. In both, the Stokes (by definition positive Raman shift,  $\Delta$ ) and anti-Stokes (negative Raman shift) parts of the spectrum [Figs. 2(a,b)] a broad maximum at  $\Delta^{\max}$  is symmetrically placed with respect to the laser line. In the 87 Å sample at excitation energy 2.54 eV [Fig. 2(c)], the maximum occurs for a small Raman shift and cannot be detected due to the finite stray-light rejection of the spectrometer. The main features of  $\Delta^{\max}$ , such as its dependence on the excitation energy for size-selective excitation, and on  $\bar{a}$  for non-resonant excitation (see Introduction and Refs. 17, 24–26), were observed in our experiments for all samples.

In the case of single-phonon processes, the Raman intensities for the Stokes,  $I_S$ , and anti-Stokes,  $I_{AS}$ , parts of the spectra are proportional to the statistical factors  $[n(\Delta) + 1]$  and  $n(\Delta)$ , where  $n(\Delta)$  is the phonon occupation number given by the Bose-Einstein distribution function:  $n(\Delta) = (\exp \Delta/kT - 1)^{-1}$ . To analyze the acoustic-mode spectra we thus divide the measured Raman intensity by the appropriate statistical factor, which is very sensitive to temperature. In order to take heating effects at the laser spot into account, the local temperature of the sample,  $T^*$ , was obtained from a fit of the experimental data to the following expression:

$$\frac{I_S(\Delta)}{I_{AS}(\Delta)} = \exp \frac{\Delta}{kT^*}. \quad (1)$$

At weak pumping powers ( $< 1$  W/cm<sup>2</sup>) the value of  $T^*$  obtained in this way is about 13 K [see lower spectra in Fig. 2(c)], close to the temperature measured by the Si diode on the sample holder in the exchange-gas cryostat ( $T=5$  K). With increased pumping power up to 25 W/cm<sup>2</sup>, however,

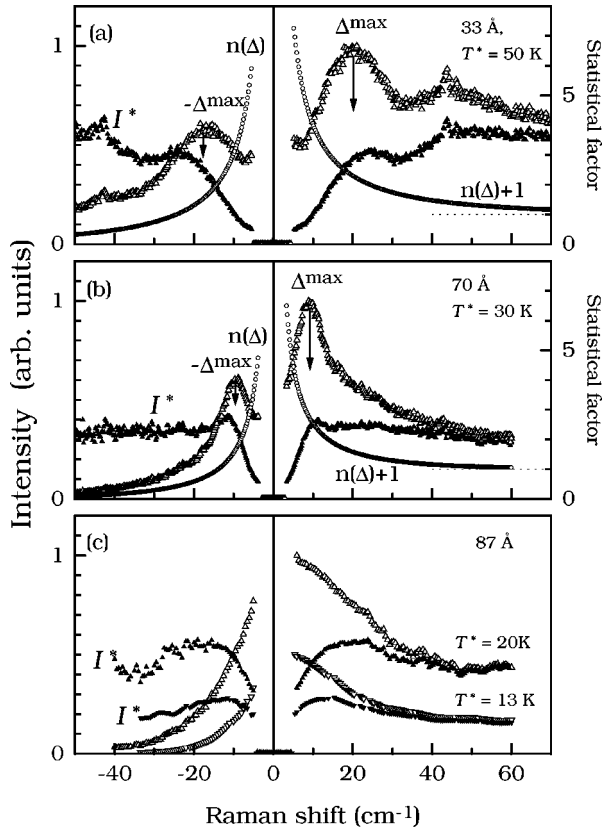


FIG. 2. APRS spectra of the CdS QD's measured in  $z(\sigma^+, \sigma^+)_z$  configuration (open triangles). (a) 33 Å,  $E_{\text{exc}}=2.7$  eV at  $T^*=50$  K. (b) 70 Å,  $E_{\text{exc}}=2.6$  eV at  $T^*=30$  K. (c) 87 Å,  $E_{\text{exc}}=2.54$  eV at  $T^*=13$  and 20 K. Stokes and anti-Stokes parts of the spectra in (a) and (b) show peaks at  $\Delta^{\text{max}}$  and  $-\Delta^{\text{max}}$ , respectively. Raman intensities  $I^*$  obtained after division of the APRS spectra by the statistical factors  $n(\Delta)$  and  $[n(\Delta)+1]$  (open circles) for the anti-Stokes and Stokes parts, respectively, are shown with filled triangles.

the effect of local heating is strong [see upper spectra in Fig. 2(c)], especially for excitation with a laser energy in the range of strong absorption. The value of  $T^*$  can reach 50 K [see Fig. 2(a)], while no change is registered by the temperature sensor. The direct measurement of the sample temperature at the laser spot by the Stokes-to-anti-Stokes ratio is therefore indispensable for an accurate analysis of the Raman line shapes and temperature-dependent measurements and values of  $T^*$  obtained this way are used throughout the paper. Note that the resonance profile for APRS is very broad compared to typical acoustic-phonon energies involved in the Raman process. Therefore, it does not affect this analysis.

Figure 2 also shows the reduced Raman intensity,  $I^*$ , obtained from the experimental spectra after dividing by the appropriate statistical factor calculated with the sample temperature  $T^*$  found from the fit to Eq. (1). As expected, the reduced spectra are nearly symmetric with respect to the laser line. This proves that APRS spectra are governed in the whole range of  $\Delta$  by first-order processes that we attribute to acoustic phonons. The spectra thus reflect the probability of scattering by one acoustic phonon. Note that a relaxation of  $\mathbf{k}$ -vector conservation is required to obtain a continuous emission over such a broad spectral range rather than the

sharp Brillouin lines that are usually observed in bulk crystals.<sup>32–36</sup> This issue will be further discussed below.

The spectral range for studies of acoustic phonons was restricted to about  $\pm 60$   $\text{cm}^{-1}$  by two factors: (i) the fast decrease of the signal in the anti-Stokes part and (ii) the appearance of a PL background in the Stokes part for larger Raman shifts. This PL background component of the total intensity in the APRS region can, in principle, have a different spectral and temperature dependence, thus producing an uncertainty in the determination of  $T^*$ . However, we obtained nearly the same value of  $T^*$  from the Stokes-to-anti-Stokes ratio of the SFRS components (see the following subsection). In the case of the very narrow SFRS lines that ratio can be measured unambiguously and, hence, it gives an even more accurate estimate of  $T^*$  compared to the above-described procedure based on the broad APRS spectra. In the following, we restrict the analysis to the range where the PL background is small compared to the APRS intensity.

It is clearly seen in Fig. 2(b), that the reduced APRS spectrum has two distinct regimes: for small phonon energies ( $\Delta < \Delta^{\text{max}}$ ),  $I^*$  increases from zero with  $\Delta$ , while for larger  $\Delta$  it decreases slowly, by about 10% between 15 and 60  $\text{cm}^{-1}$ . For the spectrum in Fig. 2(a), a similar behavior is observed. However, it corresponds to a superposition of two contributions that will be discussed below. It is significant that the broad maximum, which exists in the original spectrum, almost disappears and all that remains is a change in the slope of the spectra around  $\Delta^{\text{max}}$ . In temperature-dependent measurements we have also found that the position of  $\Delta^{\text{max}}$  increases for larger  $T$ , for example, this shift is equal to about 2  $\text{cm}^{-1}$  when  $T$  changes from 15 K to 140 K and is also reflected in the reduced spectra. In the next section we demonstrate that the maxima in Figs. 2(a,b) result from the interplay between the one-phonon scattering probability for bulk-like acoustic modes, whose exact shape needs to be established, and the phonon statistical factors.

### B. Spin-flip and acoustic-phonon Raman spectra at $B \neq 0$

In a magnetic field narrow Stokes and anti-Stokes SFRS lines appear on top of the APRS spectra [see Fig. 3(a)]. We attribute these narrow lines to acoustic-phonon-assisted electron spin-flip processes.<sup>4–7</sup> The full width at half-maximum (FWHM) of the spin-flip lines,  $\delta$ , after deconvolution with respect to the instrumental response is about 0.5  $\text{cm}^{-1}$ . This value neither changes with magnetic field nor with temperature up to 280 K. The Raman shift of the electron spin-flip line,  $\Delta^e$ , is directly proportional to  $B$ . The absolute value of the electron  $g$  factor,  $g^e$ , is related to the Zeeman splitting of the electron states by  $\Delta^e = |g^e| \mu_B B$ , where  $\mu_B$  is the Bohr magneton ( $\mu_B \approx 0.4668$   $\text{cm}^{-1}/\text{T}$ ). This dependence is shown in Fig. 4. For all samples measured, the absolute values of  $g^e$  are close to that measured for bulk CdS. In contrast to other uniaxial systems, e. g., bulk CdS (Ref. 32) or GaAs/AlAs quantum wells,<sup>7</sup> no anisotropy of the electron  $g$  factor, which would reveal itself in a dependence of the position of the spin-flip line on the orientation of the magnetic field with respect to the crystal axes or the laser beam, was observed in CdS QD's.

The APRS spectra do not depend on the magnetic field in the whole range of  $\Delta$ , while the SFRS intensity,  $I^{SF}$ , does.

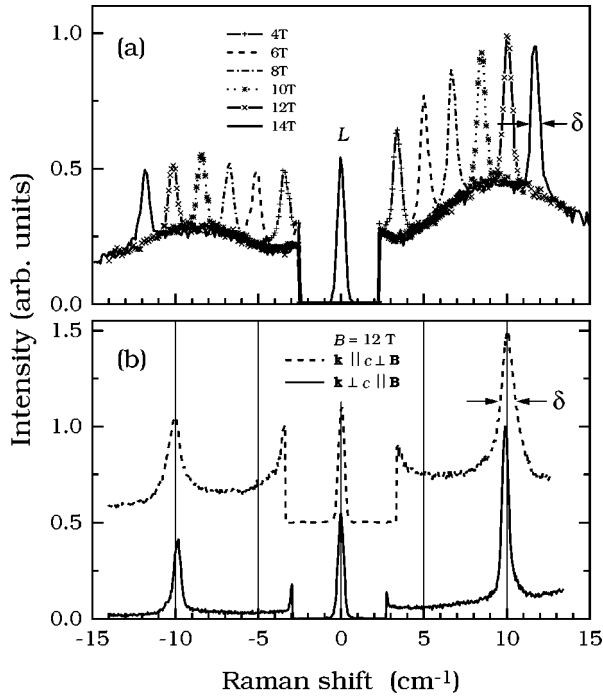


FIG. 3. (a) SFRS spectra of the 87 Å CdS QD's at different magnetic fields: ( $\mathbf{B} \parallel z$ ), measured in the parallel circular polarizations  $z(\sigma^+, \sigma^+)z$ ,  $E_{\text{exc}} = 2.6$  eV. The laser line, attenuated by a neutral density filter, is marked with  $L$ . (b) SFRS spectra for bulk CdS in the Faraday (solid line) and Voigt (dashed line) configurations. The broadening  $\delta$  of the SFRS line for  $\mathbf{k} \parallel c$  is due to exciton dispersion.

$I^{SF}$  is always proportional to the APRS intensity,  $I^{AP}$ , at the same value of  $\Delta$ . We thus conclude that  $I^{SF}$  is also related to the probability of scattering by acoustic phonons.

The polarization of SFRS has been measured for different orientations of the magnetic field with respect to the laser beam. Both the Stokes and anti-Stokes intensities exhibit the same polarization behavior. The results for the Voigt and Faraday configurations are summarized in Table I. The SFRS is strongly circularly polarized: in both configurations we find  $\rho_c \approx 0.75$ . For linearly polarized excitation in the Faraday geometry the SFRS intensity is stronger for the crossed polarizations:  $\rho_l \approx -0.5$ . Note that APRS has different polarization characteristics compared to SFRS. The degree of the linear polarization of APRS is about 0.3, and it depends only slightly on the Raman shift  $\Delta$ . No circular polarization was detected for the APRS spectra ( $\rho_c = 0$ ).

The SFRS intensity depends on the photon energy  $E_{\text{exc}}$  of the exciting laser. For example, in the 70 Å sample  $I^{SF}$  has a maximum at  $E_{\text{exc}} = 2.6$  eV and decreases when  $E_{\text{exc}}$  deviates from this value. We find that two extreme cases are realized:  $I^{AP} \gg I^{SF}$  when  $E_{\text{exc}}$  decreases and  $I^{AP} \ll I^{SF}$  when  $E_{\text{exc}}$  increases from the maximum. In other words, the resonance profile for SFRS is shifted to higher energies with respect to that of APRS. For a detailed analysis of the SFRS and APRS resonant profiles additional measurements with tunable laser excitation are required.

For each excitation energy, the intensity of both SFRS and APRS divided by the appropriate statistical factor decreases with increasing temperature as shown in Fig. 5 for the 44 and 70 Å samples and for bulk CdS. The temperature

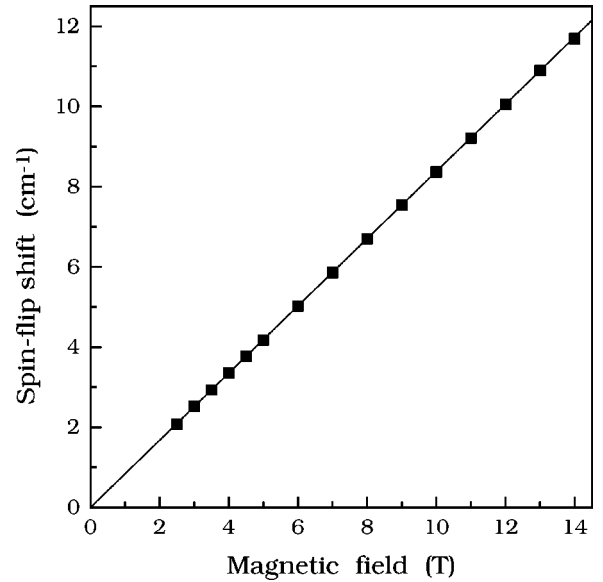


FIG. 4. Electron SFRS shift  $\Delta^e$  in the 87 Å CdS QD's vs magnetic field in the Faraday configuration,  $E_{\text{exc}} = 2.6$  eV. The solid line is a linear fit to the data.

at which the Raman intensity vanishes changes from 75 K in bulk CdS to 250 K for the 70 Å QD's. For the 33 and 44 Å QD's we did not reach the point where the Raman intensity disappears and observed only a decrease of  $I^*$  by a factor of three for an increase in temperature from 12 K to 280 K. The experimental data at high temperatures were fitted to the following expression:

$$\ln[I^*/I^*(T^* = 12\text{K})] = \frac{\varepsilon_0}{kT^*}. \quad (2)$$

Here,  $\varepsilon_0$  represents a characteristic energy obtained from the experimental curves. The fitting parameter  $\varepsilon_0$  increases with decreasing mean QD radius from 11 meV for bulk CdS to 42 meV for 44 Å QD's. For the 33 Å sample we did not reach the linear regime up to 280 K, a fact which indicates a further increase of  $\varepsilon_0$  with decreasing  $\bar{a}$ .

## IV. DISCUSSION

### A. Electron $g$ factor

We now compare the results of SFRS in CdS-based QD's to those found for bulk CdS. To do so, we have measured spectra for bulk material<sup>1,2</sup> under the same experimental conditions. In Fig. 3(b) the SFRS spectra for two orientations of a fixed magnetic field, parallel and perpendicular to the  $c$  axis of bulk CdS, are shown. We observe a slight difference in the positions of the SFRS maxima in the two configurations which reflects the anisotropy of the electron  $g$  factor. The measured components of the electron  $g$  factor tensor for magnetic fields parallel and perpendicular to the  $c$ -axis of the bulk crystal,  $g_{\parallel}^e = 1.760(5)$  and  $g_{\perp}^e = 1.785(5)$ , respectively, are represented in Fig. 6 by open squares. These values are close to those found in the literature:  $g_{\parallel}^e = 1.771(4)$  and  $g_{\perp}^e = 1.788(2)$ .<sup>32,33</sup>

The behavior of the electron  $g$  factor in QD's differs from that in bulk CdS. First, there is no macroscopic anisotropy of

TABLE I. Relative intensities of SFRS in CdS nanocrystals for Voigt ( $\mathbf{B} \perp \mathbf{k}$ ) and Faraday ( $\mathbf{B} \parallel \mathbf{k}$ ) configurations,  $B = 12 \text{ T}$ ,  $T = 5 \text{ K}$ . The symbols  $\parallel$  and  $\perp$  for linear polarization in the Voigt configurations indicate the polarization with respect to the magnetic-field direction. A comparison of the experimental intensities with the calculations for doubly resonant SFRS in  $70 \text{ \AA}$  CdS nanocrystals at  $B = 12 \text{ T}$  is also presented. The values of the normalized matrix element (NME) are calculated in terms of the weight coefficients  $a_1$ ,  $b_2$ ,  $b_3$ , and  $a_4$  involved in SFRS in the vicinity of the fundamental gap for different scattering geometries. (a) Backscattering geometry with linear polarization. (b) Backscattering geometry with circular polarization. For the Voigt configuration the quantization axis has been chosen along  $\mathbf{B}$  and the valence-band wave functions [see Eq. (7)] are modified accordingly.  $P = \langle S | p_x | X \rangle$  is the bulk momentum matrix element with  $x$  along the  $[100]$  direction.

(a)				
Linear polarization				
	$z(x,x)\bar{z}$	$z(x,y)\bar{z}$	$z(y,y)\bar{z}$	$z(y,x)\bar{z}$
<i>Voigt configuration</i>				
Experiment	$0.78_{\parallel,\parallel}$	$0.78_{\parallel,\perp}$	$0.33_{\perp,\perp}$	$1_{\perp,\parallel}$
Theory	0.78	0.5	0.6	1
NME	$-\frac{2 P ^2}{3}b_2b_3$	$\frac{-i P ^2}{\sqrt{3}}b_3$ $\times \left(a_4 + \frac{b_3}{\sqrt{3}}\right)$	$\frac{ P ^2}{2} \left(a_1 + \frac{b_2}{\sqrt{3}}\right)$ $\times \left(a_4 + \frac{b_3}{\sqrt{3}}\right)$	$\frac{-i P ^2}{\sqrt{3}}b_2$ $\times \left(a_1 + \frac{b_2}{\sqrt{3}}\right)$
<i>Faraday configuration</i>				
Experiment	0.33	1	0.33	1
Theory	0.27	1	0.27	1
NME	$\frac{ P ^2}{2} \left(a_1 - \frac{b_2}{\sqrt{3}}\right)$ $\times \left(a_4 - \frac{b_3}{\sqrt{3}}\right)$	$\frac{-i P ^2}{2} \left(a_1 - \frac{b_2}{\sqrt{3}}\right)$ $\times \left(a_4 + \frac{b_3}{\sqrt{3}}\right)$	$\frac{ P ^2}{2} \left(a_1 - \frac{b_2}{\sqrt{3}}\right)$ $\times \left(a_4 - \frac{b_3}{\sqrt{3}}\right)$	$\frac{-i P ^2}{2} \left(a_1 - \frac{b_2}{\sqrt{3}}\right)$ $\times \left(a_4 + \frac{b_3}{\sqrt{3}}\right)$
(b)				
Circular polarization				
	$z(\sigma^+, \sigma^+)\bar{z}$	$z(\sigma^+, \sigma^-)\bar{z}$		
<i>Voigt configuration</i>				
Experiment	1	0.15		
Theory	1	0.11		
NME	$-\frac{ P ^2}{4} \left(a_1 + \frac{b_3+2b_2}{\sqrt{3}}\right) \left(a_4 + \frac{b_3+2b_2}{\sqrt{3}}\right)$	$\frac{ P ^2}{4} \left(a_1 + \frac{b_3+2b_2}{\sqrt{3}}\right) \left(a_4 + \frac{b_3-2b_2}{\sqrt{3}}\right)$		
<i>Faraday configuration</i>				
Experiment	1	0.15		
Theory	1	0.1		
NME	$-\frac{1}{\sqrt{3}} P ^2a_1b_3$	$ P ^2a_1a_4$		

$g^e$  in our samples due to the random orientation of the dots and, secondly,  $g^e$  changes with decreasing excitation energy  $E_{\text{exc}}$  (or with increasing  $a^*$  according to the concept of *size-selective excitation*<sup>17</sup>) from 1.810(5) ( $E_{\text{exc}} = 2.71 \text{ eV}$ ) to 1.785(5) ( $E_{\text{exc}} = 2.54 \text{ eV}$ ), the latter value of  $g^e$  being close to that of bulk CdS. Our experimental data for electron  $g$  factors in QD's versus the excitation energy are shown in

Fig. 6 by solid symbols. At each value of  $E_{\text{exc}}$  electron  $g$  factors hardly vary from one sample to another (with different  $\bar{a}$ ) within the experimental accuracy.

In contrast to SFRS in other low-dimensional semiconductor structures,<sup>9</sup> we were not able to determine experimentally the sign of the electron  $g$  factor in CdS nanocrystals. This is a consequence of the breakdown of bulklike selection

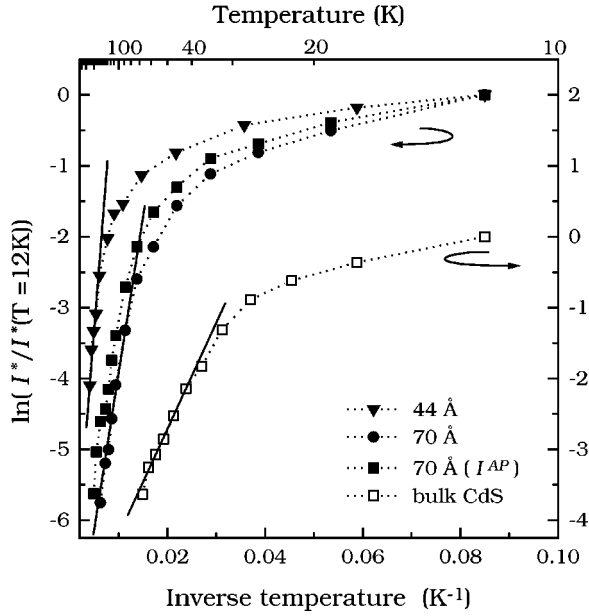


FIG. 5. Temperature dependence of the SFRS and APRS intensities  $I^*$  reduced by the appropriate statistical factor at  $\Delta = 10 \text{ cm}^{-1}$ ,  $B = 12 \text{ T}$ . The solid lines show results of the fit to Eq. (2).

rules for the polarization of the optical transitions because of the mixing of the hole states in the valence band. We have thus chosen the same (*positive*) sign for the electron  $g$  factor in the QD's as in bulk CdS.

For an accurate calculation of the electron  $g$  factor in bulk CdS a five-band  $\mathbf{k}\cdot\mathbf{p}$  method has been successfully used.<sup>11,32,34</sup> With this model, and the assumption of size-selective excitation, we can describe qualitatively the small variation of the electron  $g$  factor with  $E_{\text{exc}}$ , by replacing the fundamental gap of bulk CdS in Eq. (6) from Ref. 34 by the energy of the exciting photon. The result of this calculation, neglecting the anisotropy of the electron  $g$  factor, is shown by the solid line in Fig. 6. The main contribution to the energy dependence of  $g^e$  can be illustrated using the simple formula by Roth, Lax, and Zwerdling<sup>35</sup> which results from a three-band  $\mathbf{k}\cdot\mathbf{p}$  model:

$$g^e \approx g_0 \left[ 1 - \frac{E_p}{3} \left( \frac{1}{E} - \frac{1}{E + \Delta_0} \right) \right], \quad (3)$$

where  $g_0$  is the free-electron  $g$  factor, and  $E$  is the fundamental gap renormalized by the confinement. For *size-selective excitation*  $E$  is equivalent to  $E_{\text{exc}}$ . The values of the inter-band matrix element,  $E_p = 24.9 \text{ eV}$ , and spin-orbit splitting,  $\Delta_0 = 0.08 \text{ eV}$ , can be taken to be the same as for bulk CdS.<sup>11,32,34</sup> Due to the small value of  $\Delta_0$  in CdS (in comparison with the fundamental gap), the estimated change in  $g^e$ , when the excitation energy varies from 2.54 eV to 2.71 eV, does not exceed 1%. Note that in other nanostructures, based on semiconductors with relatively large spin-orbit splitting, significant variations of the electron  $g$  factor with size parameters were reported.<sup>8,9</sup>

We did not find any Raman signals related to spin flip of the holes, which was observed in bulk CdS for specific ori-

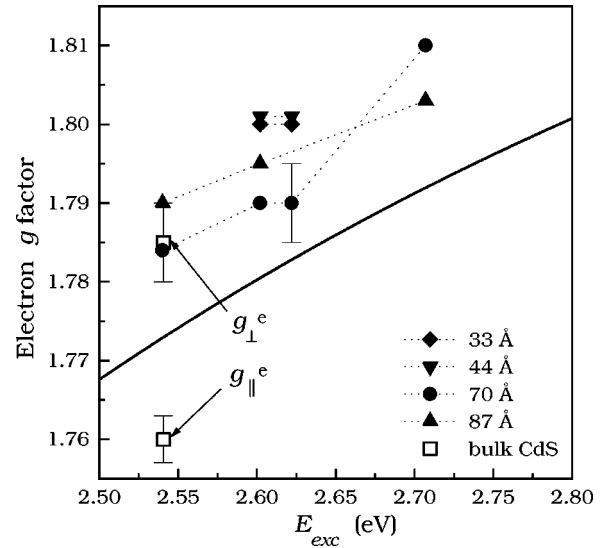


FIG. 6. Electron  $g$  factor in CdS QD's vs the excitation energy  $E_{\text{exc}}$  (solid symbols, as indicated). The two components of the electron  $g$  factor ( $g_{\parallel}^e$  and  $g_{\perp}^e$ ) for bulk CdS are shown by open squares. The solid line is the result of a five-band  $\mathbf{k}\cdot\mathbf{p}$  model calculation.

entations of the magnetic field and the  $c$  axis.<sup>1</sup> The heavy-hole  $g$  factor in CdS is strongly anisotropic due to the symmetry of the periodic part of the Bloch functions of these states.<sup>1</sup> It changes from 0 to 2.7, depending on the orientation of the magnetic field with respect to the  $c$  axis. In the case of CdS QD's, SFRS related to holes is probably absent because of a large inhomogeneous broadening in the hole Zeeman splitting, which can be of the order of the total splitting because of the random orientation of nanocrystals in the matrix.

### B. Acoustic-phonon and spin-flip Raman-scattering spectra

As already pointed out in the previous sections, the spectra of both SFRS and APRS can be explained qualitatively by the interaction of the electronic excitations *quantized in the confining potential* of the QD's with *bulklike* acoustic phonons. This effect is similar to the continuous emission ("geminate recombination") observed in bulk CdS (Ref. 36) and in GaAs/Al<sub>x</sub>Ga<sub>1-x</sub>As multiple quantum wells.<sup>37-41</sup> The appearance of a broad background signal at acoustic-phonon frequencies has been explained as the result of broken  $\mathbf{k}$ -vector conservation, induced by exciton localization in bulk CdS (Ref. 36) or by spatial confinement for the case of quantum well structures.<sup>37-41</sup> Moreover, in Ref. 36 a maximum at around  $6 \text{ cm}^{-1}$ , similar to what is shown in Figs. 2(a,b), was observed in emission spectra under resonant excitation of bulk excitons localized near impurities. The position of this maximum was determined by the characteristic size of the localized-exciton wave function, which can be viewed as an equivalent of the QD radius in the cases of strong and intermediate exciton confinement.

In QD's the electronic excitations are confined in all directions. This leads to a complete relaxation of the  $\mathbf{k}$ -vector conservation in the Raman scattering by bulk acoustic vibrations and allows us to qualitatively explain our main observations. The size distribution of the QD's needs to be taken

into account. Neglecting statistical factors, the efficiency of Raman scattering by one phonon can be written as

$$J \sim \int d\mathbf{q} da^* G(a^*) \delta(\omega_l - \omega_s - \nu q) \times \left| \sum_{\alpha, \alpha'} \frac{1}{\omega_l - \omega_\alpha(a^*, B) \pm \frac{1}{2} g \mu_B B + \frac{i}{2} \gamma_\alpha} \times M_{\alpha, \alpha'}(q, a^*) \frac{1}{\omega_s - \omega_{\alpha'}(a^*, B) \pm \frac{1}{2} g \mu_B B + \frac{i}{2} \gamma_{\alpha'}} \right|^2, \quad (4)$$

where  $G(a^*)$  is the QD size distribution function that is usually approximated by a Gaussian,  $\omega_l(\omega_s)$  is the incident (scattered) light frequency,  $\omega_\alpha(a^*, B)$  and  $\gamma_\alpha$  are the energy and the homogeneous lifetime broadening of the size-quantized electronic excitations,  $\nu$  is the average sound velocity,  $q$  a phonon wave vector, and  $M(q, a^*)$  is the matrix element of the electron-phonon interaction. In the following calculations, the width of the Gaussian dot-size distribution  $G(a^*)$  (inhomogeneous broadening) was taken to be 40% of  $\bar{a}$ .<sup>17</sup>

According to Eq. (4) the entire dispersion branches of the acoustic phonons contribute to the scattering efficiency. The relative strength of the contributions from modes with different frequencies, i.e., the scattering profile, results from a rather complicated interplay of the matrix element  $M(q, a^*)$ , the energy denominators (which can lead to resonant signal enhancement), the phonon density of states, and the QD size distribution function. However, a number of conclusions can be readily drawn from this formula. Due to the rather broad size distribution for all our samples, the main contributions to the one-phonon Raman scattering efficiency result from the processes that involve either incoming or outgoing resonance. This means that contributions to the scattering intensities in the low-energy part of the spectrum are mainly the result of the selective excitation or, for outgoing resonance, selective recombination. Model calculations according to Eq. (4) show that the scattering profile is sensitive to the dependence of the matrix element  $M(q, a^*)$  on the Raman phonon wave vector of magnitude  $q = (\omega_l - \omega_s)/\nu$ . This dependence is a product of factors corresponding to the coupling constant  $C_q$  and to the matrix element  $R(q, a^*)$  of a plane-wave  $\exp(i\mathbf{q}\mathbf{r})$  evaluated with the proper excitonic wave functions. The results of such calculations for the coupling to the acoustic vibrations via the *deformation-potential* interaction  $C_q \sim \sqrt{q}$  (see, for example, Refs. 38–41) are shown in Fig. 7(a) for three values of the homogeneous broadening parameter  $\gamma_\alpha$  equal to 0.4, 8, and 24  $\text{cm}^{-1}$ , and the QD mean radius  $\bar{a} = 40 \text{ \AA}$ . The matrix element  $R(q, a^*)$  was evaluated for transitions between  $1s$  exciton states corresponding to weak confinement, i.e., the case when the translational center-of-mass motion of the exciton is quantized while the wave function of the relative electron-hole separation coincides with that of a bulk exciton so that

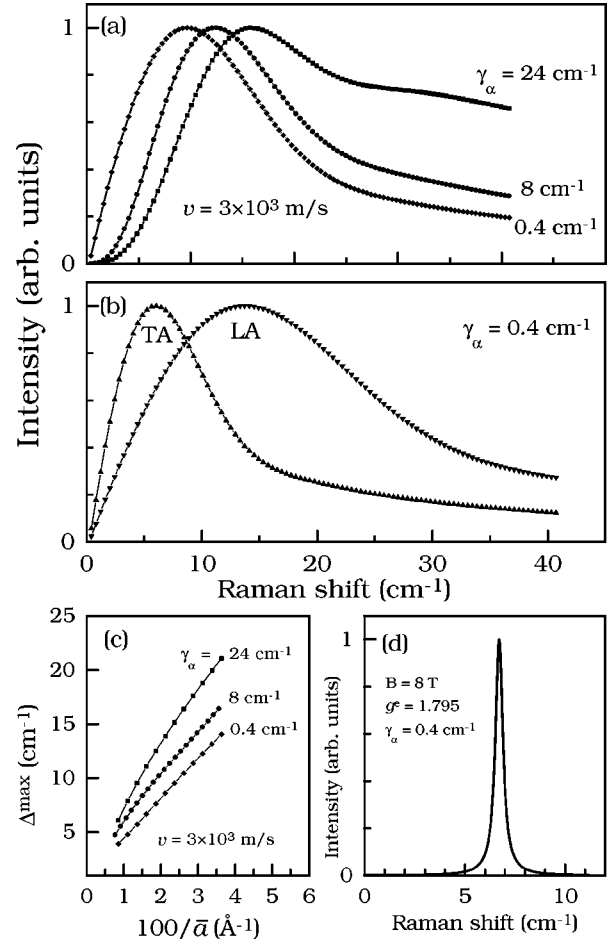


FIG. 7. Normalized Stokes Raman intensities  $J$  calculated with Eq. (4) under resonant excitation (a) for three values of the homogeneous broadening  $\gamma_\alpha = 0.4, 8,$  and  $24 \text{ cm}^{-1}$ ;  $\nu = 3 \times 10^3 \text{ m/s}$ , and  $\bar{a} = 40 \text{ \AA}$ ; (b) for two sound velocities  $\nu_{LA} = 4.25 \times 10^3 \text{ m/s}$  and  $\nu_{TA} = 1.86 \times 10^3 \text{ m/s}$ , corresponding to the *LA* and *TA* acoustic phonons in bulk CdS, and  $\bar{a} = 40 \text{ \AA}$ . (c) Calculated dependence of  $\Delta_{\max}$  on the QD radius  $\bar{a}$  for three values of  $\gamma_\alpha$ ;  $\nu = 3 \times 10^3 \text{ m/s}$ . (d) SFRS spectrum for  $B = 8 \text{ T}$  and  $g^e = 1.795$ ;  $\gamma_\alpha = 0.4 \text{ cm}^{-1}$ .

$$R(q, a^*) \sim \int_0^1 dt t^2 \frac{j_0^2(x_{0n} t)}{j_1^2(x_{0n})} j_0(q a^* t),$$

where  $j_m$  and  $x_{mn}$  are the Bessel function of order  $m$  and its  $n$ th zero, respectively. For zero magnetic field qualitative agreement with the experimental data is obtained for a broadening parameter of  $\gamma_\alpha = 24 \text{ cm}^{-1}$  [see Fig. 7(a)]. The calculated scattering efficiency  $J$  shows a rapid increase for small Raman shifts  $\Delta$  that is followed by a maximum at  $\Delta^{\max}$  and then changes to a slow decrease with a well-developed shoulder. For small  $\Delta \ll \Delta^{\max}$  and resonant excitation, the scattering efficiency mainly follows the  $q^3$  behavior that results from the product of the phonon density of states and the square of the coupling constant, while the matrix element  $R(q, a^*)$  is almost independent of  $q$ . However, for  $\Delta > \Delta^{\max}$  the strong decrease of  $R(q, a^*)$  overrules this dependence.

We thus conclude that the characteristic frequency  $\Delta^{\max}$  provides an estimate of the acoustic-phonon energy with  $q$  of the order of the typical inverse size of the size-quantized

TABLE II. Relative intensities of SFRS in bulk CdS for Voigt (**B**⊥**k**) and Faraday (**B**∥**k**) configurations,  $B=12$  T,  $T=5$  K,  $z$  is parallel to the  $c$  axis of the wurtzite CdS and  $x$  and  $y$  are two mutually orthogonal directions. The symbols ∥ and ⊥ for linear polarization in the Voigt configurations indicate the polarization with respect to magnetic-field direction. For **B**∥ $c$  in Faraday configuration, the resonant SFRS in bulk CdS is forbidden both in linear and circular polarizations,<sup>1,2</sup> which leads to a drastic decrease of the experimental intensity by two orders of magnitude in comparison with that in Voigt configuration.

	Linear polarization				Circular polarization	
	$x(y,y)\bar{x}$	$x(y,z)\bar{x}$	$x(z,z)\bar{x}$	$x(z,y)\bar{x}$	$x(\sigma^+, \sigma^+)\bar{x}$	$x(\sigma^+, \sigma^-)\bar{x}$
<b>B</b> ∥ $y$ , Voigt configuration	0.9 <sub>∥,∥</sub>	0.9 <sub>∥,⊥</sub>	0.22 <sub>⊥,⊥</sub>	1 <sub>⊥,∥</sub>	1	0.83
<b>B</b> ∥ $z$ , Voigt configuration	0.18 <sub>⊥,⊥</sub>	1 <sub>⊥,∥</sub>	0.63 <sub>∥,∥</sub>	0.79 <sub>∥,⊥</sub>	1	0.65
<b>B</b> ∥ $x$ , Faraday configuration	1	0.45	0.2	0.32	1	0.87
	$z(y,y)\bar{z}$	$z(y,x)\bar{z}$	$z(x,x)\bar{z}$	$z(x,y)\bar{z}$	$z(\sigma^+, \sigma^+)\bar{z}$	$z(\sigma^+, \sigma^-)\bar{z}$
<b>B</b> ∥ $y$ , Voigt configuration	0.63 <sub>∥,∥</sub>	1 <sub>∥,⊥</sub>	0.61 <sub>⊥,⊥</sub>	1 <sub>⊥,∥</sub>	1	0.1

exciton wave function that scales proportionally to  $1/\bar{a}$ . At  $qa^* \geq 1$  the matrix element starts to decrease due to compensation in the overlap integral of the exciton and phonon states. In the model calculations of Fig. 7(a) we took into account only one acoustic branch with an average sound velocity. The calculated dependence for  $\Delta^{\max}$  as a function of  $1/\bar{a}$  under resonant excitation is shown in Fig. 7(c) for the exciton homogeneous broadening parameters  $\gamma_\alpha = 0.4, 8,$  and  $24 \text{ cm}^{-1}$ . Note that this dependence, which is basically determined by the exciton confinement in dots with  $a^* \sim \bar{a}$ , is very similar to that predicted by the models based on confined acoustic phonons.<sup>24–27</sup> Thus most of the APRS features observed previously can also be explained by the interaction of the confined excitons with bulklike phonons. Along these arguments the observed temperature dependence of  $\Delta^{\max}$  can also be explained by the interplay of the acoustic-phonon density of states, the statistical factor, and the temperature-induced increase of  $\gamma_\alpha$  [see Fig. 7(a)], while inhomogeneous broadening of “confined” acoustic phonons does not need to be considered. Furthermore, the possibility of calculating the whole Raman spectrum, implicit in our model, should allow one to perform a more detailed comparison with the experiment than using confined acoustic modes the theoretical spectra of which are simply composed of broadened peaks at discrete vibrational eigenfrequencies.

Taking into account both longitudinal, LA, and transverse, TA, acoustic modes with different sound velocities,  $v_{LA} = 4.25 \times 10^3 \text{ m/s}$  and  $v_{TA} = 1.86 \times 10^3 \text{ m/s}$ ,<sup>42</sup> one can obtain two maxima in the Raman efficiency as shown in Fig. 7(b). The relative strength of the two contributions, which depends on the QD size,<sup>27</sup> has not been taken into account. In this scenario, the maxima at  $\Delta^{\max}$  discussed so far [see Fig. 2(a,b)] originate from TA phonons, while the second threshold at  $\Delta = 45 \text{ cm}^{-1}$  in the Raman spectrum of Fig. 2(a) corresponds to the contribution of the LA modes.

The sharp SFRS peaks observed in a high magnetic field can also be explained as involving acoustic-phonon Raman scattering<sup>4–7</sup> when the interaction Hamiltonian for transitions between the electron states with different spin<sup>43,44</sup> is taken into account (see below). Because of (i) the broad size distribution of the QD’s and (ii) the absence of **k**-vector conservation for interaction with bulk acoustic vibrations, the

SFRS peaks show up as a result of *doubly* resonant, acoustic-phonon-mediated spin-flip scattering. In contrast to the incoming or outgoing *single* resonances of APRS, which lead to the continuous emission, the SFRS involves two real intermediate states when  $\Delta$  equals the Zeeman splitting for those QD’s that are in resonance with the excitation. Note that the observed continuous dependence of the SFRS on the magnetic-field strength [Fig. 3(a)] is easily explained by the assumption of bulklike acoustic vibrations. The phonon continuum always provides phonons to fit the Zeeman splitting in a doubly resonant scattering process. This, however, cannot be directly achieved within the fully confined phonon model. The corresponding calculated SFRS spectrum is shown in Fig. 7(d) for  $B=8$  T and  $g=1.795$ . The FWHM of the calculated spin-flip line is mainly determined by the homogeneous exciton width  $\gamma_\alpha$  which was taken to be  $0.4 \text{ cm}^{-1}$  in order to reproduce the experimental spectra in Fig. 3(a). It is also slightly affected by the QD size distribution and the energy of the electronic states through Eq. (4). Note that the agreement between experimental and theoretical profiles for APRS improves for larger broadenings of the excitonic intermediate states, whereas a reasonable description of SFRS spectrum may be obtained only for a small broadening. It is difficult to describe both SFRS and APRS spectra using the same value of  $\gamma_\alpha$ , a point which needs further investigation.

We discuss now other possible mechanisms that may contribute to the broadening of the spin-flip lines in QD’s and that are not included in Eq. (4). One such contribution is related to the anisotropy of the electron  $g$  factor,  $\Delta g$ , ( $\Delta g = g_\perp^e - g_\parallel^e$ ) due to QD nonsphericity or to the wurtzite structure of each particular nanocrystal. This effect causes an additional (inhomogeneous) broadening of the spin-flip line  $\delta'$  due to an averaging over the random orientations of the QD’s in the experiment. For CdS-based QD’s this contribution, which should be linear in the magnetic field ( $\delta' \sim \Delta g \mu_B B$ ), is estimated to be about  $0.15 \text{ cm}^{-1}$ , assuming  $B=14$  T and the bulk value of  $\Delta g=0.025$ . Since no changes in  $\delta$  with  $B$  were observed within our experimental accuracy ( $0.2 \text{ cm}^{-1}$ ), we conclude that the anisotropy of the electron  $g$  factor in *each particular* QD is small and, at most, does not exceed that for bulk CdS. Comparing the SFRS spectra

in Fig. 3(a), we find that  $\delta$  for nanocrystals is smaller than for bulk CdS in case of  $\mathbf{k}\parallel c\perp B$ . The corresponding spectrum is shown by the dashed line in Fig. 3(b). Indeed, the dispersion of excitons which are intermediate states in the scattering process causes an additional broadening of the spin-flip line for excitation with a laser beam along the  $c$  axis of bulk CdS.<sup>2</sup> In QD's this mechanism is destroyed by the full exciton confinement.

### C. Selection rules for the SFRS polarization

We now discuss the selection rules for SFRS in QD's and bulk CdS. In the bulk, the SFRS polarization is determined by the resonant contributions from the A, B, and C valence subbands<sup>1,32</sup> and depends strongly on the excitation energy. The linear polarization was discussed in detail in Ref. 1. Our experimental data for bulk CdS, obtained at resonant excitation with  $E_{\text{exc}}=2.54$  eV, are summarized in Table II.

Comparing the results of Tables I and II, the polarization of the SFRS in QD's cannot be accounted for by any of the specific orientations of the crystallographic axes of bulk CdS with respect to the magnetic field and the exciting light. For example, the SFRS intensities in QD's in both the Faraday and the Voigt configurations are close to each other and the signal is strongly circularly polarized. In the bulk, the electronic SFRS is forbidden in the Faraday configuration, both in zinc-blende and wurtzite (for  $\mathbf{k}\parallel c$ ) semiconductors,<sup>1</sup> and strong but only weakly polarized in the Voigt configuration.

To describe the experimentally detected SFRS polarization in QD's (see Table I) we have calculated the appropriate matrix elements for the optical transitions. The mixing of the hole-states in the valence band due to full confinement was taken into account.<sup>45</sup> The total matrix element that determines the SFRS process in a QD can be written as

$$M^{\text{spin}} = \langle f'_e(\pm) | \mathbf{e}_s^* \cdot \mathbf{p} | \varphi_h \rangle \langle f_e(\pm) | \varphi_h | H_{e\text{-ph}}^{\text{spin}} | \varphi_h f_e(\mp) \rangle \times \langle \varphi_h | \mathbf{e}_l \cdot \mathbf{p} | f_e(\mp) \rangle, \quad (5)$$

where  $\mathbf{e}_l$  ( $\mathbf{e}_s$ ) is the polarization vector of the incoming (scattered) light,  $\mathbf{p}$  is the momentum operator,  $f_e$  and  $\varphi_h$  are the electron and hole wave functions in the QD's in a magnetic field, respectively, and  $H_{e\text{-ph}}^{\text{spin}}$  is the Hamiltonian of the spin-flip electron-phonon interaction. The  $(\pm)$  signs correspond to the electron spin orientation in the conduction band with wavefunctions  $|S\uparrow\rangle$  and  $|S\downarrow\rangle$ , respectively. Note that  $M^{\text{spin}}$  is additively included in  $M(q, a^*)$  from Eq. (4), which describes the transitions both with and without a change of the electron spin. We treat the states  $\varphi_h$  as a linear combination of the valence-band wave functions of an idealized system with zinc-blende structure, mixed at  $\mathbf{k}=0$  by size quantization:<sup>45</sup>

$$|\varphi_h\rangle = a_1|f_1, U_{hh}^+\rangle + b_2|f_2, U_{lh}^-\rangle + b_3|f_3, U_{lh}^+\rangle + a_4|f_4, U_{hh}^-\rangle. \quad (6)$$

Here,  $f_j$  ( $j=1, 2, 3,$  and  $4$ ) are the hole envelope functions for a QD in a magnetic field, and  $a_{1,4}$  and  $b_{2,3}$  are admixture coefficients that depend on the QD radius and  $B$ . The periodic parts of the Bloch wave functions in the valence band can be represented as<sup>46</sup>

$$|U_{hh}^+\rangle = \frac{|(x+iy)\uparrow\rangle}{\sqrt{2}}, \quad |U_{hh}^-\rangle = \frac{|(x-iy)\downarrow\rangle}{\sqrt{2}},$$

$$|U_{lh}^-\rangle = -\frac{1}{\sqrt{6}}|(x-iy)\uparrow\rangle - \sqrt{\frac{2}{3}}|z\downarrow\rangle, \quad (7)$$

$$|U_{lh}^+\rangle = -\frac{1}{\sqrt{6}}|(x+iy)\downarrow\rangle + \sqrt{\frac{2}{3}}|z\uparrow\rangle,$$

where  $x$ ,  $y$ , and  $z$  are orthogonal axes with respect to the laboratory frame. The spin  $|\uparrow\rangle$  ( $|\downarrow\rangle$ ) is quantized along the  $z$  axis. For a spin-flip process assisted by acoustic phonons, the matrix element of the electron-phonon interaction is<sup>43,44</sup>

$$\langle f'_e(\pm) | \varphi_h | H_{e\text{-ph}}^{\text{spin}} | \varphi_h f_e(\mp) \rangle = d\tilde{a} \left( \frac{\hbar}{\rho V v q} \right)^{1/2} \hat{\sigma}_z(\pm) \begin{pmatrix} 0 & \sigma^- \times \mathbf{q} \\ \sigma^+ \times \mathbf{q} & 0 \end{pmatrix} \times \hat{\sigma}_z(\mp) \cdot \mathbf{P}_{e,e'} \delta_{h,h'}, \quad (8)$$

where  $\hat{\sigma}_z(\mp, \pm)$  are the spin wave functions quantized along the  $z$  axis,  $\rho$  is the density,  $V$  is the normalization volume,  $\mathbf{A}=(0, xB, 0)$  is the vector potential for the external magnetic field directed along  $z$ , and  $\tilde{a}$  is the lattice constant. The expression for  $\mathbf{P}_{e,e'}$  is given by

$$\mathbf{P}_{e,e'} = \int d^3\mathbf{r} f'_e \exp(i\mathbf{q} \cdot \mathbf{r}_e) \left( \frac{\mathbf{p}}{\hbar} + \frac{e}{\hbar c} \mathbf{A} + \mathbf{q} \right) f_e. \quad (9)$$

The coupling constant  $d$  depends on the mechanism of the electron-phonon interaction. For the deformation-potential interaction<sup>43,44</sup>

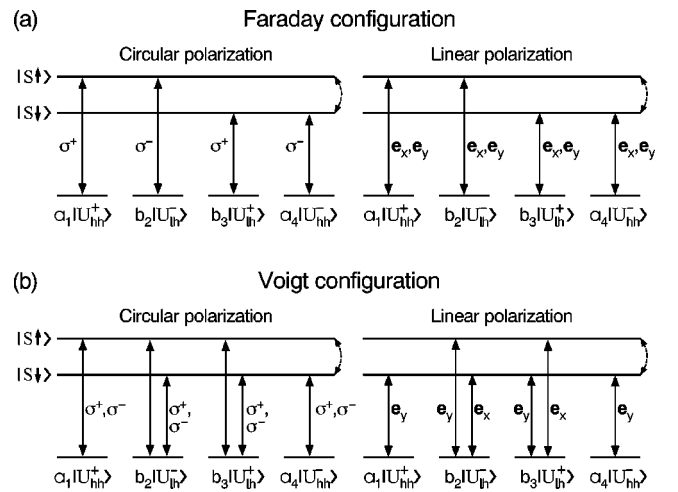


FIG. 8. Terms contributing to the Stokes and anti-Stokes SFRS in QD's in the vicinity of the fundamental gap renormalized due to confinement. The solid lines represent optical interband transitions between the conduction band ( $|S\uparrow\rangle$  and  $|S\downarrow\rangle$ ) and the mixed valence bands of heavy ( $U_{hh}^+$ ) and light ( $U_{lh}^+$ ) holes. The dashed lines represent the electron-acoustic-phonon spin-reversal transitions. (a) Transition between QD levels in the Faraday configuration ( $\mathbf{B}\parallel z, \mathbf{k}\parallel z$ ); (b) the same for the Voigt configuration ( $\mathbf{B}\parallel x, \mathbf{k}\parallel z$ ).

$$d \sim \frac{m_0}{m_e} \frac{\Delta_0}{E} d_{c,v},$$

where  $m_e$  ( $m_0$ ) is the electron effective (bare) mass, and  $d_{c,v}$  is the interband deformation potential equal to about 5 eV for bulk zinc-blende CdS.<sup>46,47</sup>

According to Eqs. (5) and (8) the spin-flip Raman scattering selection rules in QD's are determined by the nonzero products of the matrix elements  $\langle f'_e(\pm) | \mathbf{e}_s^* \cdot \mathbf{p} | \varphi_h \rangle \langle \varphi_h | \mathbf{e}_l \cdot \mathbf{p} | f_e(\mp) \rangle$  and the electron-phonon interaction. Figures 8(a,b) show the terms contributing to Stokes and anti-Stokes SFRS processes for the Faraday and Voigt configurations in the vicinity of the fundamental gap renormalized due to confinement. The spin-phonon interaction [Eq. (8)] couples a spin reversal transition (shown by dashed arrows) of the conduction electrons, thereby allowing different transitions between the heavy- and light-hole valence bands and the conduction band to contribute to the Raman scattering. The external magnetic field splits the Kramers degeneracy of the conduction band; the energy difference between two electronic states with different spin orientation can become equal to the energy of specific acoustic phonon. The incident and scattered light are simultaneously in resonance with spin reversal electronic interband transitions. Stokes and anti-Stokes SFRS processes are equal, except for a statistical phonon factor that depends on temperature.

Table I also shows the nonzero matrix elements  $\langle f_e(-) | \mathbf{e}_s^* \cdot \mathbf{p} | \varphi_h \rangle \langle \varphi_h | \mathbf{e}_l \cdot \mathbf{p} | f_e(+)\rangle$  normalized to  $\langle f_e | f_h \rangle$  for different scattering configurations which contribute to double resonant Stokes SFRS. These elements are given in terms of the coefficients  $a_1$ ,  $b_2$ ,  $b_3$ , and  $a_4$ , assuming equal oscillation

strength for each electron-hole component. The relative intensities, calculated with  $a_1/b_2=0.99$ ,  $a_1/b_3=0.826$ , and  $a_1/a_4=4.52$ , are in a good agreement with the experimental values presented in Table I for several scattering geometries. Note that the experimental data were not corrected for effects due to resonant Faraday rotation and Fresnel loss of polarization, which might cause discrepancies between the calculated and experimental data in the Table I.

## V. CONCLUSIONS

We have explained both SFRS and APRS spectra in CdS QD's through the interaction of size-quantized electronic excitations with nonconfined *bulklike* acoustic phonons. The localized character of the excitonic wave function in the quantum dots leads to the relaxation of  $\mathbf{k}$ -vector conservation in the Raman process. As a consequence, acoustic phonons throughout the entire Brillouin zone can contribute to the scattering. This leads to resonant APRS and to doubly resonant acoustic-phonon-mediated SFRS. The electron  $g$  factor in CdS QD's has been measured with high accuracy. It changes with increasing QD radius from 1.810(5) to 1.785(5), the latter value being close to that of bulk CdS.

## ACKNOWLEDGMENTS

The authors are grateful to E. L. Ivchenko, V. F. Sapega, and T. Strohm for valuable discussions. Thanks are due to P. Hiessl, H. Hirt, and M. Siemers for their help with the experiment. A. A. Sirenko and A. I. Ekimov would like to thank the Alexander von Humboldt Foundation for financial support.

\*Present address: Pennsylvania State University, 104 Davey Lab, University Park, PA 16802. Electronic address: sirenko@phys.psu.edu

- <sup>1</sup>D. G. Thomas and J. J. Hopfield Phys. Rev. **175**, 1021 (1968).
- <sup>2</sup>S. Geschwind and R. Romestain, in *Light Scattering in Solids IV*, edited by M. Cardona and G. Güntherodt, Vol. 54 of Topics in Applied Physics (Springer, Berlin, 1984), p. 151.
- <sup>3</sup>J. F. Scott, Rep. Prog. Phys. **43**, 950 (1980).
- <sup>4</sup>V. F. Sapega, M. Cardona, K. Ploog, E. L. Ivchenko, and D. N. Mirlin, Phys. Rev. B **45**, 4320 (1992).
- <sup>5</sup>D. N. Mirlin and A. A. Sirenko, Fiz. Tverd. Tela **34**, 205 (1992) [Sov. Phys. Solid State **34**, 108 (1992)].
- <sup>6</sup>V. F. Sapega, T. Ruf, M. Cardona, K. Ploog, E. L. Ivchenko, and D. N. Mirlin, Phys. Rev. B **50**, 2510 (1994).
- <sup>7</sup>A. A. Sirenko, T. Ruf, K. Eberl, M. Cardona, A. A. Kiselev, E. L. Ivchenko, and K. Ploog, in *Proceedings of the 12th International Conference on the Application of High Magnetic Fields in Semiconductor Physics*, Würzburg 1996, edited by G. Landwehr and W. Ossau (World Scientific, Singapore 1997), p. 561.
- <sup>8</sup>A. A. Sirenko, T. Ruf, M. Cardona, D. R. Yakovlev, W. Ossau, A. Waag, and G. Landwehr, Phys. Rev. B **56**, 2114 (1997).
- <sup>9</sup>A. A. Sirenko, T. Ruf, A. Kurtenbach, and K. Eberl, in *Proceedings of the 23d International Conference on the Physics of Semiconductors*, edited by M. Scheffler and R. Zimmermann (World Scientific, Singapore, 1996) p. 1385.
- <sup>10</sup>M. J. Snelling, E. Blackwood, C. J. McDonagh, R. T. Harley, and C. T. B. Foxon, Phys. Rev. B **45**, 3922 (1992).

- <sup>11</sup>M. Cardona, J. Phys. Chem. Solids **24**, 1543 (1963); C. Weisbuch and C. Hermann, Phys. Rev. B **15**, 816 (1977).
- <sup>12</sup>M. J. Snelling, G. P. Flinn, A. S. Plaut, R. T. Harley, A. C. Tropper, R. Eccleston, and C. C. Phillips, Phys. Rev. B **44**, 11 345 (1991).
- <sup>13</sup>V. K. Kalevich and V. L. Korenev, Pis'ma Zh. Eksp. Teor. Fiz. **56**, 257 (1992) [JETP Lett. **56**, 253 (1992)].
- <sup>14</sup>A. I. Ekimov and A. A. Onushchenko, Pis'ma Zh. Eksp. Teor. Fiz. **34**, 363 (1981) [JETP Lett. **34**, 345 (1981)].
- <sup>15</sup>Al. L. Éfros and A. L. Éfros, Fiz. Tekh. Poluprovodn. **16**, 1209 (1982) [Sov. Phys. Semicond. **16**, 772 (1982)].
- <sup>16</sup>A. I. Ekimov, A. A. Onushenko, and Al. L. Éfros, Solid State Commun. **56**, 921 (1985).
- <sup>17</sup>A. Ekimov, J. Lumin. **70**, 1 (1996), and references therein.
- <sup>18</sup>A. P. Alivisatos, T. D. Harris, P. J. Carrol, M. L. Steigervald, and L. E. Brus, J. Chem. Phys. **90**, 3463 (1989).
- <sup>19</sup>M. C. Klein, F. Hache, D. Ricard, and C. Flytzanis, Phys. Rev. B **42**, 11 123 (1990).
- <sup>20</sup>A. Tanaka, S. Onari, and T. Arai, Phys. Rev. B **45**, 6587 (1992).
- <sup>21</sup>E. Roca, C. Trallero-Giner, and M. Cardona, Phys. Rev. B **49**, 13 704 (1994).
- <sup>22</sup>C. Trallero-Giner, A. Debernardi, M. Cardona, E. Menéndez-Proupin, and A. I. Ekimov, Phys. Rev. B **57**, 4664 (1998).
- <sup>23</sup>P. T. C. Freire, M. A. Araújo Silva, V. C. S. Reynoso, A. R. Vaz, and V. Lemos, Phys. Rev. B **55**, 6743 (1997). Note that the authors of this work announce a future publication in which possible confinement effects will be discussed in detail.

- <sup>24</sup>E. Duval, A. Boukenter, and B. Champagnon, Phys. Rev. Lett. **56**, 2052 (1986).
- <sup>25</sup>M. Fujii, T. Nagareda, S. Hayashi, and K. Yamamoto, Phys. Rev. B **44**, 6243 (1991).
- <sup>26</sup>A. Tanaka, S. Onari, and T. Arai, Phys. Rev. B **47**, 1237 (1993).
- <sup>27</sup>T. Takagahara, J. Lumin. **70**, 129 (1996).
- <sup>28</sup>L. Saviot, B. Champagnon, E. Duval, I. A. Kudriavtsev, and A. I. Ekimov, J. Non-Cryst. Solids **197**, 238 (1996).
- <sup>29</sup>M. Lamb, Proc. Math. Soc. London **13**, 187 (1882).
- <sup>30</sup>A. Tamura, K. Higeta, and T. Ichinikawa, J. Phys. C **15**, 4975 (1982).
- <sup>31</sup>C. Weisbuch and R. G. Ulbrich, in *Light Scattering in Solids III*, edited by M. Cardona and G. Güntherodt, Vol. 51 of Topics in Applied Physics (Springer, Berlin, 1982), p. 207.
- <sup>32</sup>P. S. Kop'ev, D. N. Mirlin, V. F. Sapega, and A. A. Sirenko, Pis'ma Zh. Eksp. Teor. Fiz. **51**, 624 (1990) [JETP Lett. **51**, 708 (1990)].
- <sup>33</sup>V. F. Sapega, V. I. Belitsky, T. Ruf, H. D. Fuchs, M. Cardona, and K. Ploog, Phys. Rev. B **46**, 16 005 (1992).
- <sup>34</sup>D. N. Mirlin, I. A. Merkulov, V. I. Perel', I. I. Reshina, A. A. Sirenko, and R. Planel, Solid State Commun. **84**, 1093 (1992).
- <sup>35</sup>T. Ruf, V. I. Belitsky, J. Spitzer, V. F. Sapega, M. Cardona, and K. Ploog, Phys. Rev. Lett. **71**, 3035 (1993).
- <sup>36</sup>T. Ruf, *Phonon Raman Scattering in Semiconductors*, *Quantum Wells and Superlattices*, Vol. 142 of Springer Tracts in Modern Physics (Springer, Heidelberg, 1998).
- <sup>37</sup>C. Hermann and C. Weisbuch, Phys. Rev. B **15**, 823 (1977).
- <sup>38</sup>U. Rössler in *Numerical Data and Functional Relationships in Science and Technology*, edited by O. Madelung, Landolt-Börnstein, New Series, Group III, Vol. 22, pt. a (Springer, Berlin, 1987), p. 197.
- <sup>39</sup>M. Willatzen, M. Cardona, and N. E. Christensen, Phys. Rev. B **51**, 17 992 (1995).
- <sup>40</sup>L. M. Roth, B. Lax, and S. Zwerdling, Phys. Rev. **114**, 90 (1959).
- <sup>41</sup>J. J. Hopfield, in *Proceedings of the International Conference on the Physics of Semiconductors*, edited by A. C. Stikland (Institute of Physics and Physical Society, Exeter, 1962), p. 75.
- <sup>42</sup>D. Gerlich, J. Phys. Chem. Solids **28**, 2575 (1967).
- <sup>43</sup>S. T. Pavlov and Yu. A. Firsov, Fiz. Tverd. Tela **7**, 2635 (1965) [Sov. Phys. Solid State **7**, 2131 (1966)].
- <sup>44</sup>S. T. Pavlov and Yu. A. Firsov, Fiz. Tverd. Tela **9**, 1780 (1967) [Sov. Phys. Solid State **9**, 1394 (1967)].
- <sup>45</sup>G. B. Grigoryan, É. M. Kazaryan, Al. L. Éfros, and T. V. Yazeva, Fiz. Tverd. Tela **32**, 1772 (1990) [Sov. Phys. Solid State **32**, 1031 (1990)].
- <sup>46</sup>M. Cardona, N. E. Christensen, and G. Fasol, Phys. Rev. B **38**, 1806 (1988).
- <sup>47</sup>A. Blacha, H. Presting, and M. Cardona, Phys. Status Solidi B **126**, 11 (1984).